

SCIENTIFIC REPORTS

OPEN

Degradation pathways in standard and inverted DBP-C₇₀ based organic solar cells

Golnaz Sherafatipour¹, Johannes Benduhn², Bhushan R. Patil¹, Mehrad Ahmadpour¹, Donato Spoltore², Horst-Günter Rubahn¹, Koen Vandewal^{2,3} & Morten Madsen¹

Achieving long-term stability in organic solar cells is a remaining bottleneck for the commercialization of this otherwise highly appealing technology. In this work, we study the performance and stability differences in standard and inverted DBP/C₇₀ based organic solar cells. Differences in the charge-transfer state properties of inverted and standard configuration DBP/C₇₀ solar cells are revealed by sensitive external quantum efficiency measurements, leading to differences in the open-circuit voltages of the devices. The degradation of standard and inverted solar cell configurations at ISOS aging test conditions (ISOS-D-3 and ISOS-T-3) was investigated and compared. The results indicate that the performance drop in the small molecule bilayer solar cells is less related to changes at the D-A interface, suggesting also a pronounced morphological stability, and instead, in the case of inverted cells, dominated by degradation at the electron transport layer (ETL) bathocuproine (BCP). Photoluminescence measurements, electron-only-device characteristics, and stability measurements show improved exciton blocking, electron transport properties and a higher stability for BCP/Ag ETL stacks, giving rise to inverted devices with enhanced performance and device stability.

During the past years, organic solar cells (OSCs) have received a great deal of attention as they offer unique advantages such as low fabrication cost, semi-transparency and lightweight modules. Moreover, the power conversion efficiency (PCE) of OSCs recently reached up to 14.57%¹ and 17.3%² for single junction and tandem cells, respectively, showing the great potential of the technology. However, to be commercially viable, OSCs need to obtain long-term stabilities of at least 10 years^{3,4}, which has presented a significant challenge to this otherwise promising technology. Therefore, a deeper insight into the degradation mechanisms of the devices is needed.

In general, degradation mechanisms of OSCs can be divided into two main categories: extrinsic and intrinsic degradation. The former is caused by diffusion of water and oxygen into device layers, and the latter is due to the intrinsic nature of organic materials and involved interlayers, and includes undesirable chemical changes as well as molecular rearrangements at the device interfaces and within the active materials⁵. Encapsulation of the OSCs can significantly slow down the extrinsic degradation, while intrinsic degradation can occur even for perfectly encapsulated devices⁶⁻¹³. Relevant factors include electrode diffusion and morphological changes, resulting in a complex range of degradation mechanisms, which imply that the interface between every two adjacent layers has a strong impact on the stability of the devices¹⁴. In organic solar cells, one of the critical places for intrinsic degradation is the interface between the electron donating (D) and accepting (A) material where chemical and morphological changes over time directly affect photogeneration of charge carriers and recombination processes. Residing at the D-A interface, the charge-transfer (CT) state mediates the charge carrier separation and the free charge carrier recombination, and its properties directly affect the device performance, especially the open-circuit voltage (V_{OC})¹⁵⁻¹⁷. Furthermore, degradation paths are rather complex and differ between standard and inverted stack architectures¹⁸⁻²¹. For example, Krebs *et al.* and Cros *et al.* reported that for the two types of architectures, with the same type of photoactive layer and identical processing procedure, the inverted configuration devices show a higher air stability^{22,23}. This however depends on the exact type of layer stack used, and cannot be used as a general rule. Specific interlayers may also lead to different stability trends for standard and inverted device

¹SDU NanoSYD, Mads Clausen Institute, University of Southern Denmark, Sønderborg, Denmark. ²Dresden Integrated Center for Applied Physics and Photonic Materials (IAPP) and Institute for Applied Physics Technische Universität Dresden Nöthnitzer Str. 61, 01187, Dresden, Germany. ³Present address: Institute for Materials Research (IMO-IMOME), Hasselt University, Wetenschapspark 1, 3590, Diepenbeek, Belgium. Correspondence and requests for materials should be addressed to M.M. (email: madsen@mci.sdu.dk)

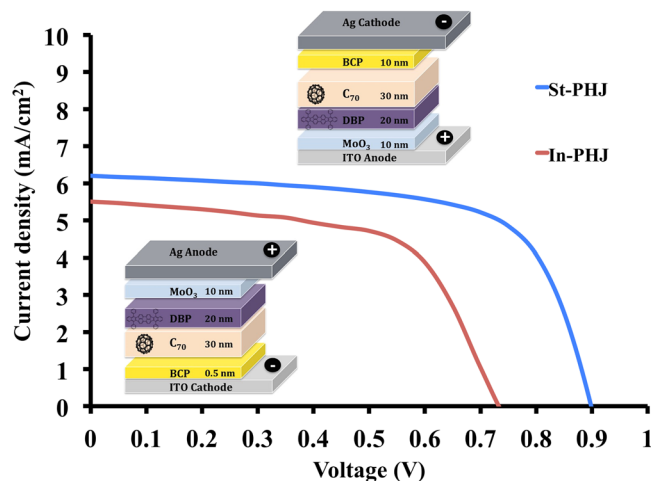


Figure 1. J-V scans of DBP/C₇₀ organic based planar heterojunction (PHJ) devices having standard (St-PHJ) and inverted (In-PHJ) device configurations.

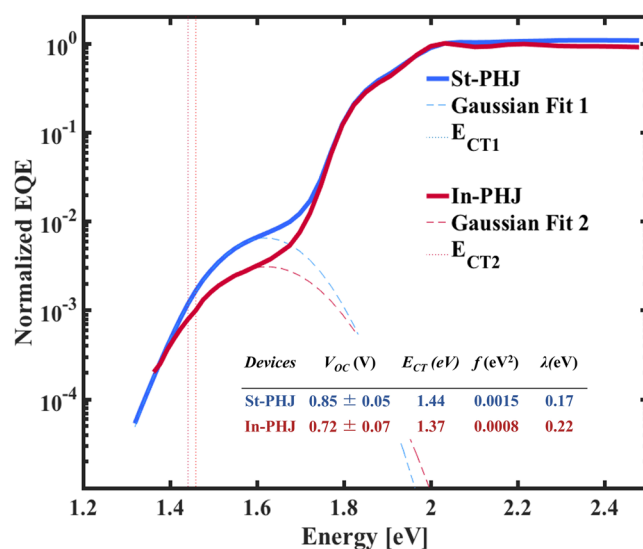


Figure 2. sEQE measurements and Marcus fits for standard and inverted solar cells (solid lines) as a function of the photon energy. Dashed lines show Gaussian fits to the low energy part of the sEQE spectrum, using Marcus theory.

Device type	V_{oc} (V)	J_{sc} (mA/cm ²)	PCE (%)	FF (%)
St-PHJ	0.85 ± 0.05	6.32 ± 0.36	3.66 ± 0.21	68.0 ± 1.8
In-PHJ	0.72 ± 0.07	5.78 ± 0.40	2.68 ± 0.29	62.0 ± 2.5

Table 1. OSC performance parameters of DBP/C₇₀ organic based PHJ devices having standard (St-PHJ) and inverted (In-PHJ) device configurations. The reported values are averaged from the extracted measurements of total 7 devices of each type.

architectures. For example, the hole transport layer molybdenum oxide has been shown to lead to more stable device performance than PEDOT:PSS hole transport layers in standard configuration devices²⁴, whereas the exact opposite is the case in inverted configuration cells²⁵. This sets the need for an individual lifetime assessment of any new layer stack embedded in OPV technology.

In this work, we investigate degradation pathways in Tetrphenyldibenzoperiflanthen (DBP) and Fullerene (C₇₀) based organic solar cells, having standard and inverted device architectures. DBP is a promising electron donor material, which has been utilized in organic solar cells since 2009^{26–34}. Its advantages, such as high optical absorption strength and deep highest occupied molecular orbital (HOMO) level around 5.5 eV makes it a good

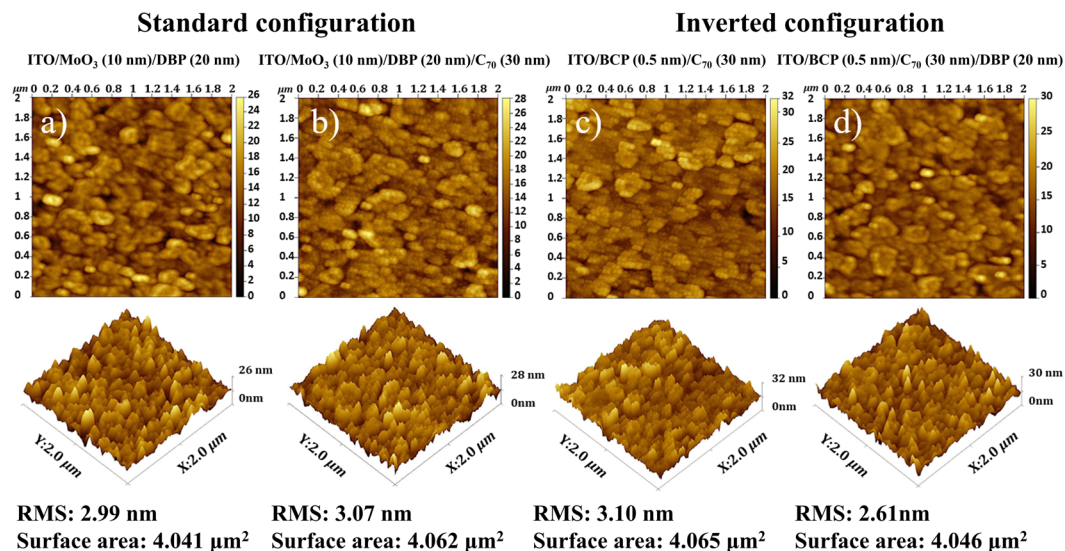


Figure 3. AFM images of interface layer (a) ITO/MoO₃ (10 nm)/DBP (20 nm), (b) ITO/MoO₃/DBP (20 nm)/C₇₀ (30 nm), (c) ITO/BCP (0.5 nm)/C₇₀ (30 nm), and (d) ITO/BCP (0.5 nm)/C₇₀ (30 nm)/DBP (20 nm).

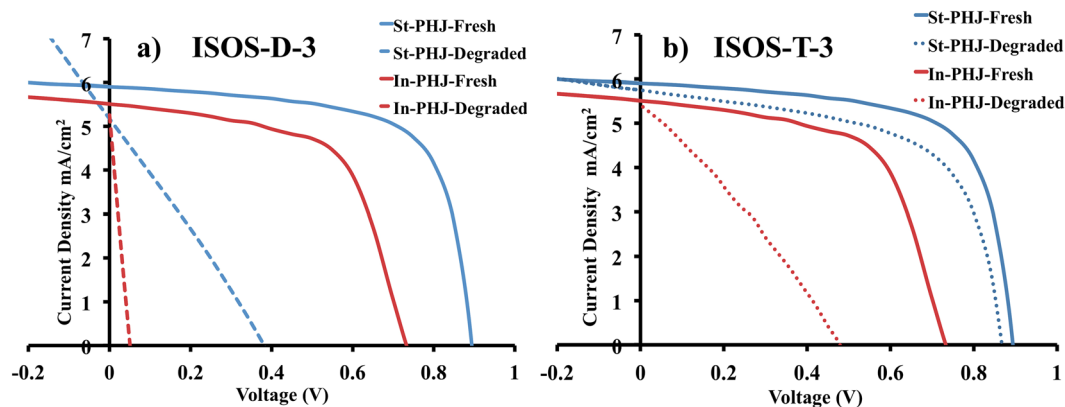


Figure 4. J-V curves for fresh standard (blue) and inverted (red) devices (solid lines) and aged devices (dashed lines) at (a) ISOS-D-3 (b) and ISOS-T-3 degradation conditions.

Devices	V _{OC} (V)	J _{SC} (mA/cm ²)	PCE (%)	FF (%)
St-Fresh	0.85 ± 0.05	5.8 ± 0.26	3.50 ± 0.17	71.2 ± 1.1
In-Fresh	0.72 ± 0.07	5.88 ± 0.57	2.68 ± 0.29	62.0 ± 2.5
St-ISOS-D-3	0.36 ± 0.28	4.90 ± 1.44	0.68 ± 0.73	23.3 ± 16.7
In-ISOS-D-3	0.03 ± 0.05	5.60 ± 0.54	0.01 ± 0.02	7.3 ± 14.5
St-ISOS-T-3	0.87 ± 0.05	5.67 ± 0.34	2.94 ± 0.52	59.3 ± 6.7
In-ISOS-T-3	0.45 ± 0.07	5.86 ± 0.93	1.02 ± 0.55	37.9 ± 13.8

Table 2. Photovoltaic performance parameters of fresh and aged devices under ISOS-D-3 and ISOS-T-3 degradation conditions. Device parameters for standard configuration are marked in blue, and for inverted device configuration in red.

match to fullerene acceptors, resulting in reasonably high open-circuit voltages^{31,35–39}. We use sensitive external quantum efficiency (sEQE) measurements to detect morphological differences between standard and inverted device configurations, and to detect potential degradation at the DBP/C₇₀ interface after aging the devices at ISOS-D-3 (darkness, 80 °C, 85% relative humidity (RH)) and ISOS-T-3 (darkness, −40 °C, ambient humidity) aging conditions. Our findings show that despite the changes in V_{OC} values of the fresh and degraded devices, CT state properties undergo only very minor changes, suggesting a pronounced morphological stability at the

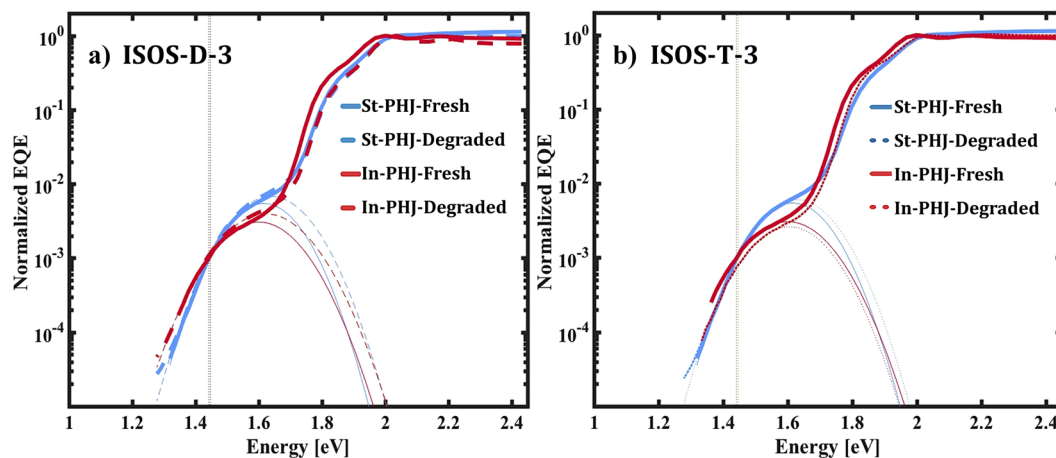


Figure 5. sEQE measurements and Marcus fits for fresh and aged devices at (a) ISOS D-3 and (b) ISOS-T-3 conditions.

Devices	V_{OC} (V)	f (eV ²)	λ (eV)	E_{CT} (eV)
St-PHJ-Fresh	0.85 ± 0.05	0.0017	0.17	1.44
In-PHJ-Fresh	0.72 ± 0.07	0.0008	0.22	1.37
St-PHJ-ISOS-D-3	0.36 ± 0.28	0.0017	0.19	1.44
In-PHJ-ISOS-D-3	0.03 ± 0.05	0.0011	0.23	1.38
St-PHJ-ISOS-T-3	0.87 ± 0.05	0.0014	0.18	1.44
In-PHJ-ISOS-T-3	0.45 ± 0.07	0.0006	0.20	1.40

Table 3. V_{OC} and CT parameters extracted through fits of sEQE spectra for fresh and aged devices at ISOS-D-3 and ISOS-T-3 degradation conditions. Device parameters for standard configuration are marked in blue, and for inverted device configuration in red.

DBP/C₇₀ interface. Instead, it is demonstrated that the inverted devices suffer from higher V_{OC} losses and low stability due to the use of a Bathocuproine (BCP) electron transport layer (ETL)⁴⁰. To address this challenge, we introduce a BCP/Ag stack as an alternative ETL with improved carrier transport efficiency and exciton blocking properties. Our final results show that inverted devices implementing BCP/Ag stacks as ETL lead to enhanced device stabilities.

Results and Discussion

The J-V characteristics of the standard and inverted devices with identical contacts and active layers are presented in Fig. 1 and Table 1. The parameters, shown in Table 1, are averaged over 7 devices of each type, and J-V curves in Fig. 1 show devices with characteristics closest to the average parameters.

Although both device types have identical active layers, the devices based on the standard structure show an overall better performance, reaching 130 mV higher V_{OC} and higher PCE. Recent work has demonstrated that this trend, however, may depend on device area⁴¹. We note that the reported performances here are similar to those reported for bilayer DBP/C₇₀ cells in the literature^{32,42}.

Previous studies have shown that morphological differences and changing molecular orientation at the D-A interface can lead to V_{OC} changes by altering the material energy levels⁴³ and the properties of the CT states. We investigate the differences in V_{OC} of the devices through the sEQE measurements and CT state characteristics. Based on the electron transfer theory developed by Marcus^{44,45}, energy of the CT state (E_{CT}), the reorganization energy (λ), and the amplitude of the CT absorption band (f) are determined by fitting the low energy part of the EQE spectrum with a Gaussian, using the method outlined in reference¹⁵. We obtain that E_{CT} is 1.44 eV for the standard and 1.37 eV for the inverted device configuration. The normalized sEQE spectra and their corresponding fits and extracted CT state parameters are shown in Fig. 2.

The 70 meV higher E_{CT} in the standard configuration is in agreement with the higher V_{OC} value obtained, although it does not explain the full change in V_{OC} upon inverting the structure. A slightly higher f value is also obtained for the standard configuration, which identifies as a higher density of CT states, being correlated to a higher amount of interface between the donor and acceptor molecules¹⁷. Previous findings indicate that a larger interface area results in a higher recombination current⁴⁶; however, the difference in f value seen here is minor, and should not contribute to significant V_{OC} differences. Atomic force microscopy (AFM) images were recorded for the top layers in (a) ITO/MoO₃/DBP, (b) ITO/MoO₃/DBP/C₇₀, (c) ITO/BCP/C₇₀, and (d) ITO/BCP/C₇₀/DBP stacks, as shown in Fig. 3, in order to investigate further the morphology at the interface. The first

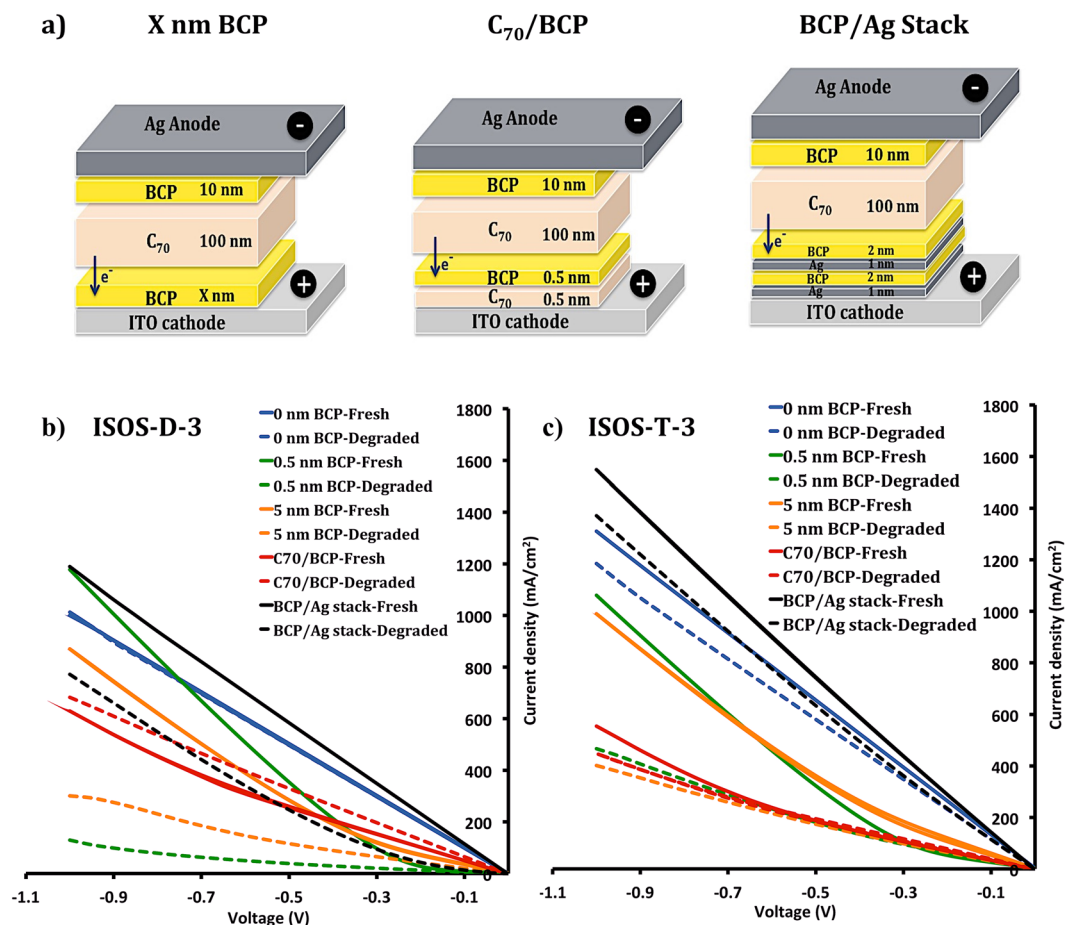


Figure 6. (a) Electron-only devices with different ETLs. J-V measurements after aging devices for 24 hours in (b) ISOS-D-3 and (c) ISOS-T-3 degradation conditions.

two and the second two stacks represent the layers in standard and inverted configurations, respectively. The root-mean-square (RMS) roughness and surface area values were extracted and are shown in Fig. 3.

Figure 3a,c show the surfaces of the lower layer of the D-A interface in each type of device. In the standard configuration (Fig. 3a), the DBP layer has a slightly smoother surface with lower surface area, although very close to what is seen for the inverted configuration. This could imply that a non-conformal film coverage for DBP on the C₇₀ layer lead to the slightly lower *f* value seen for the inverted device configuration. In general we note that variations in molecular orientations can impact voltage losses, charge generation efficiency, and CT properties^{43,47–50}, and that both a modified interface area and modified molecular orientation can lead to the slightly different *f* values observed here.

Figure 4 shows the J-V characteristics of the fresh cells and cells degraded in ISOS-D-3 and ISOS-T-3 conditions for 24 hours. Average values over 7 devices of each set are presented in Table 2.

Under ISOS-D-3 condition, the PCE values drop significantly for both devices, although it is most significant for inverted cells. The PCE drop is mostly the consequence of a reduction in FF and *V*_{OC} values, which may be due to an increase in the density of deeper traps caused by oxidation of the active layer^{51–53}. These traps can act as recombination centers and disturb the distribution of the internal field⁵². Furthermore, metal diffusion from the top contacts into the buffer layer at the high temperature can also result in a decreased FF^{54,55}.

For the ISOS-T-3 condition, the PCE value of the standard devices is less influenced by this aging condition and the *V*_{OC} value remains intact. This could be due to the slowed down chemical reactions taking place in the organic materials at the low temperatures used. This effect from temperature is demonstrated in the Supplementary Information in Fig. S-1, where degradation of encapsulated standard devices in ISOS-T-3 and ISOS-D-1 (darkness, room temperature) conditions are compared. We observe that for ISOS-T-3 condition, the *V*_{OC} of the devices remains above 80% of its initial value after 3500 hours. However, for devices kept at room temperature (ISOS-D-1), the *T*₈₀ point is reached much earlier, at around 500 hours^{15,56}. However, looking at the results for inverted devices in the same condition (Fig. 4), a notable change in the device stability is seen as compared to the standard configuration cells. Since the same material system is present in both types of devices, this is an indication of a degradation process not related to standard photo-oxidation of the active layer. Under ISOS-D-3 conditions, when humidity and high temperature are included, degradation is accelerated and effects from both chemical reactions in the active layer and instabilities of the interlayers are seen resulting in pronounced degradation.

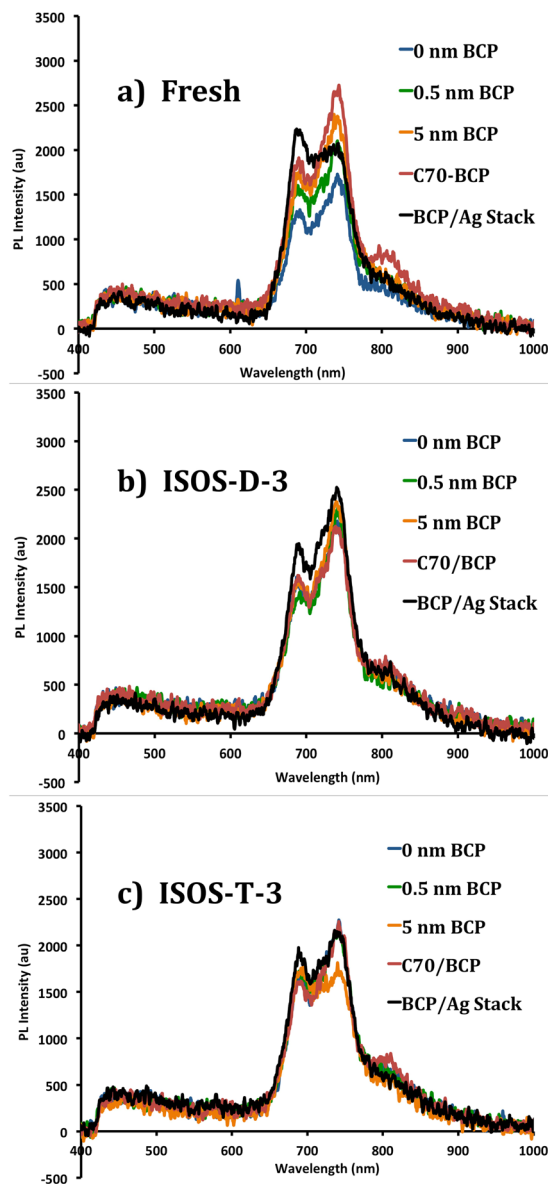


Figure 7. Photoluminescence (PL) measurements for five ETLs, measured “fresh” and degraded at ISOS-D-3 and ISOS-T-3. The BCP/Ag stack has the structure: BCP (2 nm)/Ag (1 nm)/BCP (2 nm)/Ag (1 nm)/BCP (2 nm).

In order to detect possible morphological changes at the D-A interface, sEQE measurements were performed for degraded samples as well. Figure 5 shows normalized sEQE spectra and their corresponding fits for fresh and aged devices at each aging condition. Table 3 presents the extracted CT parameters.

The sEQE results indicate that although a change in V_{OC} of the devices is measured after degradation, the CT properties remain almost the same. The unchanged f value indicates a morphological stability at the DBP/ C_{70} interface, suggesting that a drop in voltage upon aging of the devices is not due to morphological changes at the D-A interface. This is furthermore supported by investigations on annealing of standard PHJ and Bulk Heterojunction devices (BHJ), which was conducted at 110 °C for 3 hours inside a glovebox in darkness (see Supplementary Information, Fig. S.2). The results show that although a significantly larger f value is seen for the BHJ cells, as expected, no change in CT state energy and f value is seen upon degradation of these devices.

For the inverted configuration, the C_{70} absorption (shoulder at 1.8 eV) drops slightly relative to DBP absorption during degradation. We attribute this instability of C_{70} to changes in the underlying BCP layer. It has been shown that BCP can be employed as an ETL in inverted devices, but this can lead to problems in device performance with low FF and PCE⁴⁰, depending on the device area⁴¹. Moreover, it can give rise to V_{OC} losses at the ETL- C_{70} interface due to its tendency for crystallization and inducing defects⁴¹.

In the standard device architecture, an Ag-BCP complex is formed due to diffusion of the Ag into the BCP layer⁵⁷. This complex can facilitate electron transport by introducing a new lowest unoccupied molecular orbital (LUMO) level aligned with the LUMO of the C_{70} ⁵⁸. However, the inverted structure lacks this BCP-metal complex and thus efficient electron extraction⁵⁹. For the small device areas of 10 mm² investigated here, reasonable

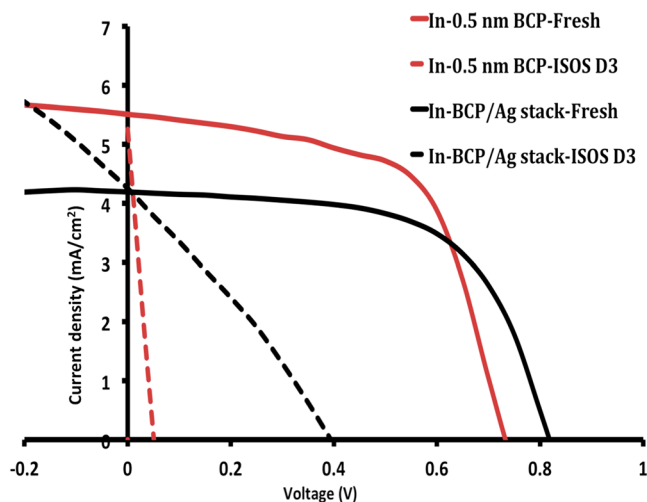


Figure 8. J-V measurements for fresh and aged inverted device with 0.5 nm BCP (ITO/BCP (0.5 nm)/C₇₀ (30 nm)/DBP (20 nm)/MoO₃ (10 nm)/Ag (100 nm)) and BCP/Ag stack (ITO/BCP (2 nm)/Ag (1 nm)/BCP (2 nm)/Ag (1 nm)/BCP (2 nm)/C₇₀ (30 nm)/DBP (20 nm)/MoO₃ (10 nm)/Ag (100 nm)).

ETL	V _{OC} (V)	J _{SC} (mA/cm ²)	PCE (%)	FF (%)
0.5 nm BCP-Fresh	0.72 ± 0.07	5.78 ± 0.40	2.68 ± 0.29	62.0 ± 2.5
0.5 nm BCP-ISOS-D-3	0.04	5.26	0.062	26.2
BCP/Ag stack-Fresh	0.82 ± 0.05	4.19 ± 0.16	2.09 ± 0.13	60.4 ± 4.1
BCP/Ag stack-ISOS-D-3	0.37	4.25	0.48	30.2

Table 4. Photovoltaic characteristics of fresh and aged inverted devices with 0.5 nm BCP or BCP/Ag stack as their hole transport layer.

device efficiencies for inverted architectures are observed, but with limited device stability. In order to investigate the instabilities further, we assessed the ETL properties of several thicknesses of BCP and two BCP ETL stacks based on C₇₀ and Ag in an inverted configuration. It has been shown that an ultrathin layer of C₇₀ between ITO and BCP can improve the ETL properties and the device yield⁴¹. The second candidate can provide a BCP-Ag semi-complex without directly doping the BCP layer.

Electron transport properties of the implemented ETLs were examined via electron-only devices (EODs) (see Fig. 6a and methods), for both fresh and aged devices. In these devices, electrons are injected into the devices through the Ag electrode and extracted at the ITO side. Figure 6b,c show EOD characteristics after degrading the devices at ISOS-D-3 and T-3 conditions for 24 hours. J-V measurements for the fresh EODs show a lower series resistance for the BCP/Ag stack, indicating better electron transport properties. Interestingly, devices without BCP layer at the bottom (0 nm BCP) show no or very minor degradation, indicating that indeed the BCP layer is responsible for the degradation in the inverted cells. Note that these devices have a top BCP layer, and the results show a high stability for this layer and no major role in the degradation of the devices. The results also show that pure BCP hampers electron extraction in this inverted configuration, as expected due to the lack of a metal-BCP complex.

The exciton blocking properties of the ETLs were examined using photoluminescence (PL) measurements. The results presented in Fig. 7a demonstrate that increasing the BCP thickness increases the PL intensity of the C₇₀ layer, due to increased exciton blocking of the ETL and thus minimum quenching at the cathode interface.

The stability of these electron transport layers were tested by aging the samples at ISOS-D-3 and ISOS-T-3 conditions for 24 hours, and repeating the PL measurements after the aging process. Figure 7b,c represent the results for each condition. The results show overall lower PL intensities in both standard and inverted configurations comparing degraded to fresh films. However, in each set, the BCP/Ag stack shows better exciton blocking properties with higher PL intensities. From these results we conclude that the BCP/Ag stack both provides improved exciton blocking and electron transport properties, and also less interface degradation. Therefore, we implemented this ETL candidate in full inverted devices, and evaluated the device performance and stability.

Inverted devices with the BCP/Ag stack were fabricated with the structure ITO/(BCP/Ag stack)/C₇₀/DBP/MoO₃/Ag. J-V curves were recorded under 1 sun illumination for fresh and degraded devices in ISOS-D-3 condition, and compared with the previous results for 0.5 nm BCP as ETL. The results are presented in Fig. 8 and Table 4.

The obtained results show improved V_{OC} and stability for the BCP/Ag stack ETL based devices, demonstrating that the BCP ETL is causing the initial larger V_{OC} drop for inverted cells, along with the accelerated degradation compared to the standard configuration devices. Since the J-V measurements are performed through

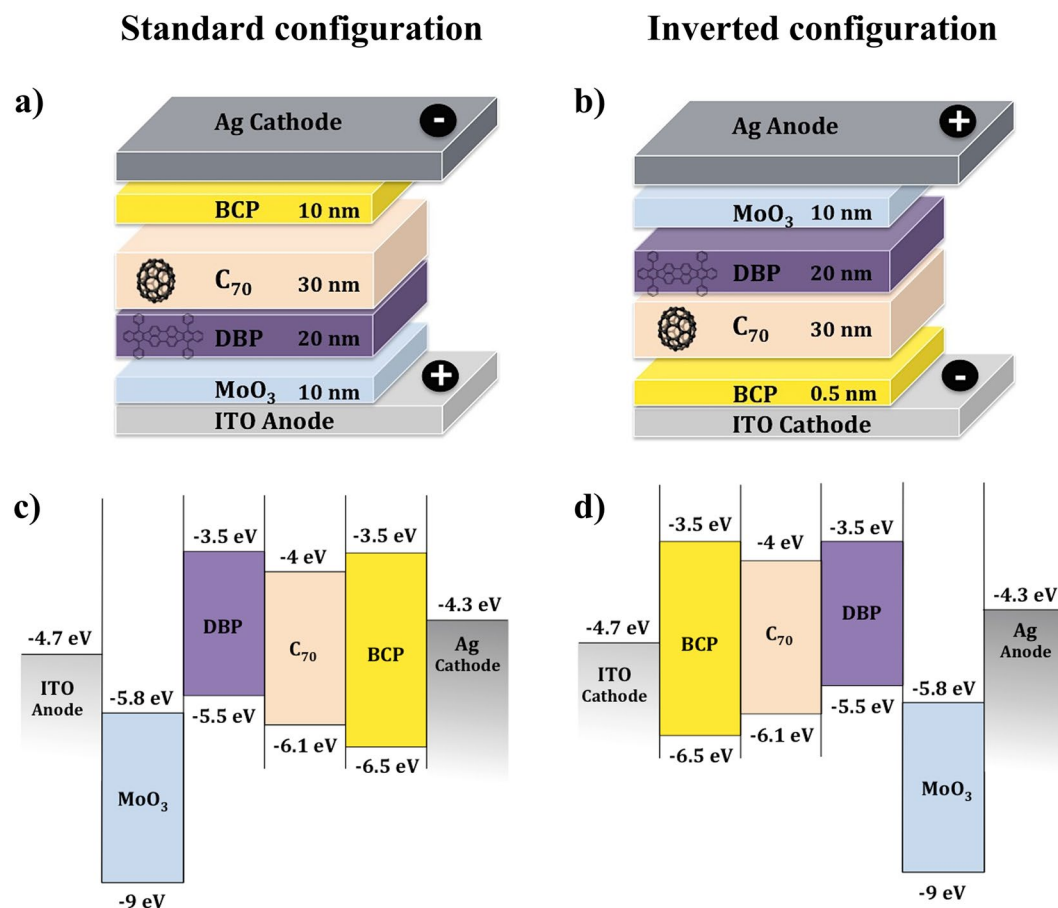


Figure 9. Device architecture of (a) standard, and (b) inverted structure of the fabricated organic solar cells. Energy level diagram^{26,28} of (c) standard and (d) inverted DBP/ C_{70} based devices.

a bottom illumination, a slightly lower J_{SC} is resulting from a reflection from the thin layer of Ag at the ETL. Interestingly, the performance of the ISOS-D-3 degraded BCP/Ag based inverted cells show similar performance as the ISOS-D-3 degraded standard configuration cells, indicating that the interlayer now possesses a similar stability as the one implemented in the standard configuration devices. A similar strong improvement in the stability of DBP/ C_{70} organic solar cell devices upon improving the molybdenum oxide hole transport layer was recently demonstrated, also pointing to the importance on the stability of the contact layer in such solar cell devices⁶⁰.

In this work, the performance and stability of DBP- C_{70} based organic solar cells in standard and inverted device configurations were studied. Although differences in V_{OC} between standard and inverted devices were observed for fresh cells, the results revealed no morphological or CT state changes at the DBP- C_{70} interface upon degradation in ISOS-D-3 and ISOS-T-3 conditions. Instead, the different ISOS degradation measurements were pointing at electrode or interlayer instabilities being a significant cause of degradation in inverted devices, which was backed up by investigations of the effect of the ETL on device stability. The results demonstrate that this layer is contributing significantly to the observed degradation of the inverted devices. Different BCP film thicknesses and two BCP based ETL stacks were evaluated from PL measurements and electron-only devices. The results show improved performance and a higher device stability for inverted devices based on a BCP/Ag stack as electron transport layer, which thus point to pure BCP being the weak point in the stability of these devices.

Methods

Solar cells studied in this work were fabricated using DBP as electron donor and C_{70} as electron acceptor. For electron transport and hole transport layers, BCP and molybdenum oxide (MoO_3) were used, respectively. Silver (Ag) (AESpump ApS, Denmark) was used as top electrode in both types of devices. DBP was purchased from Luminescence Technology Corp., Taiwan, and C_{70} , MoO_3 and BCP were purchased from Sigma-Aldrich, Germany. Solar cell devices were fabricated on pre-coated, pre-patterned indium-tin oxide (ITO) glass substrates with a sheet resistance of 9–15 Ω/sq (purchased from University wafer, Inc, USA). The used device stacks are shown in Fig. 9. Standard PHJ devices have the architecture: ITO/ MoO_3 (10 nm)/DBP (20 nm)/ C_{70} (30 nm)/BCP (10 nm)/Ag (100 nm), and inverted PHJ devices: ITO/BCP (0.5 nm)/ C_{70} (30 nm)/DBP (20 nm)/ MoO_3 (10 nm)/Ag (100 nm). Standard bulk heterojunction (BHJ) devices were obtained from co-evaporation of DBP and C_{70} materials with 1:1 deposition ratio, having the architecture: ITO/ MoO_3 (10 nm)/DBP: C_{70} (80 nm)/BCP (10 nm)/Ag (100 nm).

Prior to fabrication of the OSC devices, the ITO substrates were cleaned using detergent, acetone, and isopropanol in an ultrasonic water bath (10 min each) and blow-dried with a nitrogen gun. Next, the substrates were treated by plasma cleaning for 20 min, and transferred to a glovebox connected cluster deposition system, which has a base vacuum pressure below 10^{-8} mbar. In this system, the organic material layers, metal oxide interlayers, and metal electrodes were sequentially deposited without breaking vacuum in between the steps. Shadow masks were employed to define the OSC cell area of 10 mm^2 . The deposition rates for the organic materials and Ag top electrode were kept at 0.3 \AA/s and 0.5 \AA/s , respectively.

The *J-V* characteristics of the OSCs were recorded in ambient conditions using a calibrated 3000 class AAA solar simulator from Abet Technologies Inc., USA connected to a Keithley 2400 source measure unit (Keithley instruments Inc., USA). The *J-V* characteristics were measured by applying a voltage sweep between $+1$ to -0.25 V using a lamp intensity of 100 mW/cm^2 .

sEQE measurements. Light from a quartz Halogen lamp (50 W) was chopped at 140 Hz and spectrally dispersed by a monochromator (Cornerstone 260 1/m, Newport), and then directed onto the mounted sample. The produced current at the short-circuit condition was pre-amplified and converted into a voltage signal. Then the signal was analyzed by a LOCK-IN-amplifier ((7280 DSP, Signal Recovery, Oak Ridge, USA) to measure only the frequency modulated signal. EQE was calculated as the ratio of the photocurrent to flux of the incoming photons (obtained by a calibrated silicon and/or indium-gallium-arsenide photodiode)⁶¹. The time constant of the LOCK-IN amplifier was set to 1 s to achieve a span spectrum over 5–7 decades, and its amplification was increased to resolve low photocurrents. The sEQE spectra of the devices were analyzed by fitting the low-energy range by employing a home-developed MATLAB code.

Degradation measurements. For the stability assessment, a climate chamber with 85°C and 85% RH (in darkness), and a thermal chamber at -40°C , room humidity, and darkness were used to simulate ISOS-D-3 and ISOS-T-3 degradation protocols, respectively. Devices were placed inside each condition for 24 hours, after which *J-V* characteristics were recorded using the solar simulator under 1 sun illumination.

Morphological characterization. AFM images were recorded, using a Veeco Dimension 3100 scanning probe microscope in tapping mode. Vacuum deposition of each sample was performed without breaking the vacuum between the layers, and images were recorded in air directly after fabrication.

PL quenching measurements. A fluorescence microscope (Nikon Eclipse ME600) with a microscope objective (Nikon E Plan $50 \times 0.75 \text{ EPL}$) connected to a Maya2000Pro Spectrometer (from Ocean optics) was used to record the spectra. A mercury short arc lamp having a filtered excitation wavelength centered between 330–380 nm was used as light source. The PL signal was collected with a 10 s integration time, and measurements were repeated after aging the devices as per ISOS test protocols.

Space-charge limited current (SCLC) measurements on electron-only devices. Electron-only devices were fabricated by sandwiching the C_{70} layer between the respective bottom ETL and top BCP/Ag contact, using the same deposition rates as for solar cell device fabrication. ITO was used as bottom electrodes. *J-V* characteristics of the devices were recorded by applying a sweeping voltage between $+1$ and -1 V at reverse bias using a Keithley 2400 source measure unit, directly following fabrication and repeated after aging the devices.

References

- Zheng, Z. *et al.* A Highly Efficient Non-Fullerene Organic Solar Cell with a Fill Factor over 0.80 Enabled by a Fine-Tuned Hole-Transporting Layer. *Adv. Mater.* **30**, 1801801 (2018).
- Meng, L. *et al.* Organic and solution-processed tandem solar cells with 17.3% efficiency. *Science*. **361**, 1094–1098 (2018).
- Mulligan, C. J. *et al.* A projection of commercial-scale organic photovoltaic module costs. *Sol. Energy Mater. Sol. Cells* **120**, 9–17 (2014).
- Azzopardi, B. *et al.* Economic assessment of solar electricity production from organic-based photovoltaic modules in a domestic environment. *Energy Environ. Sci.* **4**, 3741 (2011).
- Cao, H. *et al.* Recent progress in degradation and stabilization of organic solar cells. *J. Power Sources* **264**, 168–183 (2014).
- Yang, X., Van Duren, R. A. J., Janssen, J. K. J., Michels, M. A. J. & Loos, J. Morphology and Thermal Stability of the Active Layer in Poly(p-phenylenevinylene)/Methanofullerene Plastic Photovoltaic Devices. *Macromolecules* **37**, 2151–2158 (2004).
- Zhao, J. *et al.* Phase Diagram of P3HT/PCBM Blends and Its Implication for the Stability of Morphology Phase Diagram of P3HT/PCBM Blends and Its Implication for the Stability of Morphology. *J. Phys. Chem. B* **113**, 1587–1591 (2009).
- Bertho, S. *et al.* Influence of thermal ageing on the stability of polymer bulk heterojunction solar cells. *Sol. Energy Mater. Sol. Cells* **91**, 385–389 (2007).
- Vandenbergh, J. *et al.* Thermal stability of poly[2-methoxy-5-(2'-phenylethoxy)-1,4-phenylenevinylene] (MPE-PPV):Fullerene bulk heterojunction solar cells. *Macromolecules* **44**, 8470–8478 (2011).
- Ning, Y. *et al.* Investigation on Thermal Degradation Process of Polymer Solar Cells Based on Blend of PBDTTT-C and PC 70 BM. *Int. J. Photoenergy*. **2014**, 354837 (2014).
- Kesters, J. *et al.* Enhanced organic solar cell stability by polymer (PCPDTBT) side chain functionalization. *Chem. Mater.* **27**, 1332–1341 (2015).
- Turkovic, V. *et al.* Long-term stabilization of organic solar cells using UV absorbers. *J. Phys. D: Appl. Phys.* **49**, 125604 (2016).
- Turkovic, V. *et al.* Long-term stabilization of organic solar cells using hydroperoxide decomposers as additives. *Appl. Phys. A*. **122**, 255 (2016).
- Ecker, B. *et al.* Degradation effects related to the hole transport layer in organic solar cells. *Adv. Funct. Mater.* **21**, 2705–2711 (2011).
- Vandewal, K., Tvingstedt, K., Gadisa, A., Inganäs, O. & Manca, J. V. Relating the open-circuit voltage to interface molecular properties of donor:acceptor bulk heterojunction solar cells. *Phys. Rev. B - Condens. Matter Mater. Phys.* **81**, 125204 (2010).
- Zou, Y. & Holmes, R. J. Correlation between the Open-Circuit Voltage and Charge Transfer State Energy in Organic Photovoltaic Cells. *ACS Appl. Mater. Interfaces* **7**, 18306–18311 (2015).

17. Vandewal, K., Tvingstedt, K., Manca, J. V. & Inganäs, O. Charge-Transfer States and Upper Limit of the Open-Circuit Voltage in Polymer:Fullerene Organic Solar Cells. *IEEE J. Sel. Top. Quantum Electron.* **16**, 1676–1684 (2010).
18. Nam, S. *et al.* Inverted polymer fullerene solar cells exceeding 10% efficiency with poly(2-ethyl-2-oxazoline) nanodots on electron-collecting buffer layers. *Nat. Commun.* **6**, 8929 (2015).
19. Dey, S., Vivo, P., Efimov, A. & Lemmetyinen, H. Enhanced performance and stability of inverted organic solar cells by using novel zinc-benzothiazole complexes as anode buffer layers. *J. Mater. Chem.* **21**, 15587 (2011).
20. Lee, S.-H., Seo, J.-W. & Lee, J.-Y. Stable inverted small molecular organic solar cells using a p-doped optical spacer. *Nanoscale* **7**, 157–165 (2015).
21. Lan, J.-L. *et al.* The effects of Ta₂O₅-ZnO films as cathodic buffer layers in inverted polymer solar cells. *J. Mater. Chem. A* **2**, 9361–9370 (2014).
22. Krebs, F. C., Gevorgyan, S. A. & Alstrup, J. A roll-to-roll process to flexible polymer solar cells: model studies, manufacture and operational stability studies. *J. Mater. Chem.* **19**, 5442 (2009).
23. Cros, S. *et al.* Definition of encapsulation barrier requirements: A method applied to organic solar cells. *Sol. Energy Mater. Sol. Cells* **95**, S65–S69 (2011).
24. Sun, Y. *et al.* Efficient, air-stable bulk heterojunction polymer solar cells using MoOx as the anode interfacial layer. *Adv. Mater.* **23**, 2226–2230 (2011).
25. Hermerschmidt, F. *et al.* Influence of the Hole Transporting Layer on the Thermal Stability of Inverted Organic Photovoltaics Using Accelerated-Heat Lifetime Protocols. *ACS Appl. Mater. Interfaces* **9**, 14136–14144 (2017).
26. Fujishima, D. *et al.* Organic thin-film solar cell employing a novel electron-donor material. *Sol. Energy Mater. Sol. Cells* **93**, 1029–1032 (2009).
27. Che, X., Xiao, X. & Forrest, S. R. Highly Efficient (11.1%) Small Molecule Multi-junction Organic Photovoltaic. *Cells* **70**, 140–142 (2014).
28. Hirade, M. & Adachi, C. Small molecular organic photovoltaic cells with exciton blocking layer at anode interface for improved device performance. *Appl. Phys. Lett.* **99**, 2009–2012 (2011).
29. Yokoyama, D. *et al.* High-efficiency simple planar heterojunction organic thin-film photovoltaics with horizontally oriented amorphous donors. *Sol. Energy Mater. Sol. Cells* **98**, 472–475 (2012).
30. Zheng, Y. *et al.* Highly efficient bulk heterojunction photovoltaic cells based on C₇₀ and tetraphenylidibenzoperiflanthene. *Appl. Phys. Lett.* **102**, 143304 (2013).
31. Xiao, X., Zimmerman, J. D., Lassiter, B. E., Bergemann, K. J. & Forrest, S. R. A hybrid planar-mixed tetraphenylidibenzoperiflanthene/C₇₀ photovoltaic cell. *Appl. Phys. Lett.* **102**, 073302 (2013).
32. Wang, Z. *et al.* Highly efficient organic p-i-n photovoltaic cells based on tetraphenylidibenzoperiflanthene and fullerene C₇₀. *Energy Environ. Sci.* **6**, 249–255 (2013).
33. Ahmadpour, M., Liu, Y., Rubahn, H. G. & Madsen, M. Current Matching in Multifold DBP/C₇₀ Organic Solar Cells with Open-Circuit Voltages of up to 6.44 V. *IEEE J. Photovolt.* **7**, 1319–1323 (2017).
34. Patil, B. R., Liu, Y., Qamar, T., Rubahn, H. G. & Madsen, M. 4P-NPD ultra-thin films as efficient exciton blocking layers in DBP/C₇₀ based organic solar cells. *J. Phys. D: Appl. Phys.* **50**, 385101 (2017).
35. Wang, Z. *et al.* High fill factor and thermal stability of bilayer organic photovoltaic cells with an inverted structure. *Appl. Phys. Lett.* **106**, 053305 (2015).
36. Peng, Y., Zhang, L. & Andrew, T. L. High open-circuit voltage, high fill factor single-junction organic solar cells. *Appl. Phys. Lett.* **105**, 083304 (2014).
37. Nazeeruddin, M. K. *et al.* Conversion of Light to Electricity by cis-X₂Bis(2,2'-bipyridyl-4,4'-dicarboxylate) ruthenium (II) Charge-Transfer Sensitizers (X = Cl⁻, Br⁻, I⁻, CN⁻, and SCN⁻) on Nanocrystalline TiO₂ Electrodes. *J. Am. Chem. Soc.* **115**, 6382–6390 (1993).
38. Horvath, H. Atmospheric light absorption - a review. *Atmos. Environ. Part A, Gen. Top.* **27**, 293–317 (1993).
39. Zhuang, T., Sano, T. & Kido, J. Efficient small molecule-based bulk heterojunction photovoltaic cells with reduced exciton quenching in fullerene. *Org. Electron. physics, Mater. Appl.* **26**, 415–419 (2015).
40. Hao, X. *et al.* Novel cathode buffer layer of Ag-doped bathocuproine for small molecule organic solar cell with inverted structure. *Org. Electron. physics, Mater. Appl.* **15**, 1773–1779 (2014).
41. Patil, B. R. *et al.* Area dependent behavior of bathocuproine (BCP) as cathode interfacial layers in organic photovoltaic cells. *Sci. Rep.* **8**, 12608 (2018).
42. Galindo, S. *et al.* Influence of the density of states on the open-circuit voltage in small-molecule solar cells. *Org. Electron. physics. Mater. Appl.* **15**, 2553–2560 (2014).
43. Hörmann, U. *et al.* Voc from a Morphology Point of View: the Influence of Molecular Orientation on the Open Circuit Voltage of Organic Planar Heterojunction Solar Cells. *J. Phys. Chem. C* **118**, 26462–26470 (2014).
44. Marcus, R. A. Relation between charge transfer absorption and fluorescence spectra and the inverted region. *J. Phys. Chem.* **93**, 3078–3086 (1989).
45. Gould, I. R., Farid, S., Noukakis, D., Goodman, J. L. & Young, R. H. A Quantitative Relationship between Radiative and Nonradiative Electron Transfer in Radical-Ion Pairs. *J. Am. Chem. Soc.* **115**, 3830–3831 (1993).
46. Vandewal, K. *et al.* Increased open-circuit voltage of organic solar cells by reduced donor-acceptor interface area. *Adv. Mater.* **26**, 3839–3843 (2014).
47. Zheng, Y. *et al.* Comparative investigation of molecular orientation and charge collection in highly efficient mixed heterojunctions based on three planar-shaped donors and C₇₀. *J. Phys. D: Appl. Phys.* **49**, 465106 (2016).
48. Ran, N. A. *et al.* Impact of interfacial molecular orientation on radiative recombination and charge generation efficiency. *Nat. Commun.* **8**, 79 (2017).
49. Fu, Y. T. *et al.* Structure and disorder in squaraine-C₆₀ organic solar cells: A theoretical description of molecular packing and electronic coupling at the donor-acceptor interface. *Adv. Funct. Mater.* **24**, 3790–3798 (2014).
50. Zimmerman, J. D. *et al.* Independent control of bulk and interfacial morphologies of small molecular weight organic heterojunction solar cells. *Nano Lett.* **12**, 4366–4371 (2012).
51. Seemann, A. *et al.* Reversible and irreversible degradation of organic solar cell performance by oxygen. *Sol. Energy* **85**, 1238–1249 (2011).
52. Schafferhans, J., Baumann, A., Wagenpfahl, A., Deibel, C. & Dyakonov, V. Oxygen doping of P3HT:PCBM blends: Influence on trap states, charge carrier mobility and solar cell performance. *Org. Electron. physics, Mater. Appl.* **11**, 1693–1700 (2010).
53. Hauch, J. A., Schilinsky, P., Choulis, S. A., Rajoelson, S. & Brabec, C. J. The impact of water vapor transmission rate on the lifetime of flexible polymer solar cells. *Appl. Phys. Lett.* **93**, 103306 (2008).
54. Guerrero, A. & Garcia-Belmonte, G. Recent advances to understand morphology stability of organic photovoltaics. *Nano-Micro Lett.* **9**, 10 (2017).
55. Kim, H. J., Lee, H. H. & Kim, J. J. Real time investigation of the interface between a P3HT:PCBM layer and an Al electrode during thermal annealing. *Macromol. Rapid Commun.* **30**, 1269–1273 (2009).
56. Cardinaletti, I. *et al.* Organic and perovskite solar cells for space applications. *Sol. Energy Mater. Sol. Cells* **182**, 121–127 (2018).
57. Vogel, M., Doka, S., Breyer, C., Lux-Steiner, M. C. & Fostiropoulos, K. On the function of a bathocuproine buffer layer in organic photovoltaic cells. *Appl. Phys. Lett.* **89**, 163501 (2006).

58. Yoshida, H. Electron Transport in Bathocuproine Interlayer in Organic Semiconductor Devices. *J. Phys. Chem. C* **119**, 24459–24464 (2015).
59. Tong, X., Lassiter, B. E. & Forrest, S. R. Inverted organic photovoltaic cells with high open-circuit voltage. *Org. Electron. physics, Mater. Appl.* **11**, 705–709 (2010).
60. Ahmadpour, M *et al.* Crystalline molybdenum oxide layers as efficient and stable hole contacts in organic photovoltaic devices. *ACS Appl. Energy Mater.* **2**, 420–427 (2019).
61. Graham, K. *et al.* Charge-transfer state energy determines open-circuit voltage in organic photovoltaics. *SPIE Newsroom*, <https://doi.org/10.1117/2.1201309.005006> (2013).

Acknowledgements

The research leading to these results has received funding from the People Programme (Marie Curie Actions) of the European Union's Seventh Framework Programme FP7/2007–2013/under REA Grant Agreement No. 607232, THINFACE. J.B., D.S. and K.V. acknowledge the German Federal Ministry for Education and Research (BMBF) for funding the project through the InnoProfile project “Organische p-i-n Bauelemente 2.2”.

Author Contributions

G.Sh. and M.M. conceived the idea. G.Sh., J.B., D.S., K.V. and M.M. designed the experiments. G.Sh. performed device fabrication and characterization. B.R.P. contributed to optimization of inverted devices and performed device fabrication for annealing tests. M.A. optimized the standard devices. J.B. and G.Sh. conducted sensitive external quantum efficiency measurements. G.Sh. conducted film and electron-only device characterization as well as the device degradation measurements. The work was carried out under the supervision of H.G.R., K.V. and M.M. G.Sh. formulated the initial manuscript, and all co-authors participated in the exchange and analyses of the results as well as in the editing the manuscript.

Additional Information

Supplementary information accompanies this paper at <https://doi.org/10.1038/s41598-019-40541-6>.

Competing Interests: The authors declare no competing interests.

Publisher's note: Springer Nature remains neutral with regard to jurisdictional claims in published maps and institutional affiliations.



Open Access This article is licensed under a Creative Commons Attribution 4.0 International License, which permits use, sharing, adaptation, distribution and reproduction in any medium or format, as long as you give appropriate credit to the original author(s) and the source, provide a link to the Creative Commons license, and indicate if changes were made. The images or other third party material in this article are included in the article's Creative Commons license, unless indicated otherwise in a credit line to the material. If material is not included in the article's Creative Commons license and your intended use is not permitted by statutory regulation or exceeds the permitted use, you will need to obtain permission directly from the copyright holder. To view a copy of this license, visit <http://creativecommons.org/licenses/by/4.0/>.

© The Author(s) 2019